

A Small Deformation Thermoporomechanics Finite Element Model and Its Application to Arterial Tissue Fusion

D. P. Fankell

Department of Mechanical Engineering,
University of Colorado Boulder,
Boulder, CO 80309

R. A. Regueiro

Department of Civil, Environmental,
and Architectural Engineering,
University of Colorado Boulder,
Boulder, CO 80309

E. A. Kramer

Department of Mechanical Engineering,
University of Colorado Boulder,
Boulder, CO 80309

V. L. Ferguson

Department of Mechanical Engineering,
University of Colorado Boulder,
Boulder, CO 80309

M. E. Rentschler¹

Department of Mechanical Engineering,
University of Colorado Boulder,
1111 Engineering Drive UCB 427,
Boulder, CO 80309
e-mail: mark.rentschler@colorado.edu

Understanding the impact of thermally and mechanically loading biological tissue to suprphysiological levels is becoming of increasing importance as complex multiphysical tissue–device interactions increase. The ability to conduct accurate, patient specific computer simulations would provide surgeons with valuable insight into the physical processes occurring within the tissue as it is heated or cooled. Several studies have modeled tissue as porous media, yet fully coupled thermoporomechanics (TPM) models are limited. Therefore, this study introduces a small deformation theory of modeling the TPM occurring within biological tissue. Next, the model is used to simulate the mass, momentum, and energy balance occurring within an artery wall when heated by a tissue fusion device and compared to experimental values. Though limited by its small strain assumption, the model predicted final tissue temperature and water content within one standard deviation of experimental data for seven of seven simulations. Additionally, the model showed the ability to predict the final displacement of the tissue to within 15% of experimental results. These results promote potential design of novel medical devices and more accurate simulations allowing for scientists and surgeons to quickly, yet accurately, assess the effects of surgical procedures as well as provide a first step toward a fully coupled large deformation TPM finite element (FE) model. [DOI: 10.1115/1.4037950]

Keywords: finite element modeling, biomechanics, thermoporomechanics, poromechanics, bioheat transfer, tissue fusion

1 Introduction

Biological tissue undergoes thermal loading in several manners ranging from surgical devices that heat or cool biological tissue to cauterize or ablate it [1–4], to natural causes such as hyperthermia or frostbite [5]. Scientists and physicians seek to understand these processes and their impact on tissue mechanics to create novel, safer, and more effective medical devices and procedures. With tissue–device interaction becoming ever more prevalent in the form of more complex medical devices, wearable electronics, and implanted electronics, experimental testing is becoming increasingly expensive in time and resources. Computer simulations of these interactions, when calibrated to experimental data, provide essential insight into the underlying physics occurring in biological tissue when deformed and heated, allowing for streamlined design work and ultimately more effective devices and safer procedures. Additionally, models with the ability to accurately and quickly predict surgical outcomes will help satisfy the growing desire for patient specific, near real time, simulations for surgical procedures [6].

A good deal of biological tissue is nonhomogenous and typically contains several materials, often in different phases [5]. For example, the artery wall has an extracellular matrix (ECM) made up of collagen, elastin, and glycosaminoglycans. While water is attracted to molecules within the tissue through polar interactions, it readily moves through interstitial spaces. Thus, this tissue can

be considered as a porous medium. Studies attempting to model biological tissue, including vertebral disks [7], articular cartilage [8], lung tissue [9], arterial tissue [10], skin [5], tumor [5], and myocardial tissue [11] as a porous medium exist throughout literature; however, these attempts have failed to completely represent the complex physics occurring within the tissue. Typically, models representing biological tissue as porous media fall into one of two categories. The first neglects deformation and only heat and/or mass transfer is represented [3,5,12]. The second category of models uses solid mechanics and mass transport to model tissue deformation and coupled pore fluid flow, but thermal transport is not considered [7,9,13]. To the authors' knowledge, no model exists that demonstrates the coupled solid phase (ECM) mechanics, mass transfer, and heat transfer (thermoporomechanics (TPM)) occurring in biological tissue. In this paper, a small deformation, TPM finite element (FE) model with the ability to represent the heating and deformation of biological tissue is presented, and its results are validated by comparison to measured experimental results of thermal arterial tissue fusion.

2 Methods

2.1 Initial Definitions. Throughout this paper, it will be assumed that the biological tissue being modeled will be partially saturated triphasic (also called unsaturated) porous media. Meaning the tissue will consist of some solid skeletal matrix and multiple fluid constituents (gas and liquid) occupying the voids between the solid matrix. It will be assumed the voids will be filled with liquid water and gaseous water vapor all tissue is

¹Corresponding author.

Manuscript received June 20, 2017; final manuscript received September 14, 2017; published online January 17, 2018. Assoc. Editor: Ram Deviredy.

avascular, meaning the tissue itself does not contain blood vessels or lymphatic vessels that could act as source/sink for fluid.

To fully describe a partially saturated triphasic porous medium, several definitions must be prescribed and constraints given. Considering a total differential volume, dv , with a total differential mass, dm , it can be said that the total differential volume and mass are equal to a sum of the differential volumes and masses of each phase, α (s = solid, ℓ = liquid, g = gas), at a continuum point

$$dv = \sum_{\alpha=s,\ell,g} dv_{\alpha} \quad (1)$$

$$dm = \sum_{\alpha=s,\ell,g} dm_{\alpha} \quad (2)$$

Thus, we can define the volume fraction of each phase, n^{α} , as

$$n^{\alpha} = \frac{dv_{\alpha}}{dv} \quad (3)$$

With Eq. (3), it can be seen that

$$1 = n^s + n^{\ell} + n^g = n^s + n \quad (4)$$

where n is the volume fraction of the pore space, or porosity. The differential mass of each phase can be written as

$$dm_{\alpha} = \rho^{\alpha R} dv_{\alpha} = \rho^{\alpha R} n^{\alpha} dv \quad (5)$$

where $\rho^{\alpha R}$ is the true (real) mass density of the α phase. With Eq. (5), it can be shown that the partial mass density, ρ^{α} , is

$$\rho^{\alpha} = \rho^{\alpha R} n^{\alpha} \quad (6)$$

Finally, it is beneficial to define the saturation of the liquid and gas phases, S_f , as the volume fraction of the pore space occupied by each fluid phase

$$S_f = \frac{n^f}{n}, \quad f = l, g \quad (7)$$

$$1 = S_{\ell} + S_g \quad (8)$$

2.2 Kinematics. To fully understand the physical processes occurring within porous media when loaded, it is necessary to examine the kinematics of a volume element and its constituents. From fundamental continuum mechanics and the theory of porous media [14,15], it can be said that each phase undergoes some motion, χ_{α} , defined as

$$\mathbf{x} = \chi_{\alpha}(\mathbf{X}_{\alpha}, t) \quad (9)$$

where \mathbf{x} is the current “smeared” position of all phases at time, t and \mathbf{X}_{α} is the initial location of the α phase as shown in Fig. 1. Thus, the deformation gradient, \mathbf{F}_{α} , for the α phase is

$$\mathbf{F}_{\alpha} = \frac{\partial \chi_{\alpha}(\mathbf{X}_{\alpha}, t)}{\partial \mathbf{X}_{\alpha}} = \frac{\partial \mathbf{x}(\mathbf{X}_{\alpha}, t)}{\partial \mathbf{X}_{\alpha}} \quad (10)$$

Examining the volumetric change of the differential volume element, it is seen that

$$dv = J_{\alpha} dV_{\alpha} \quad (11)$$

$$dv_{\alpha} = n^{\alpha} J_{\alpha} dV_{\alpha} \quad (12)$$

where J_{α} is the determinant of the deformation gradient, \mathbf{F}_{α} , and dV_{α} is the reference differential volume for the α phase. These are nonlinear geometric, or large deformation, variables, but we will simplify later to the linear (small deformation) theory.

2.3 Governing Equations. Three governing equations will be used in the finite element formulation: balance of mass, balance of linear momentum, and balance of energy for the three phase mixture. While these equations can be arranged to solve for numerous

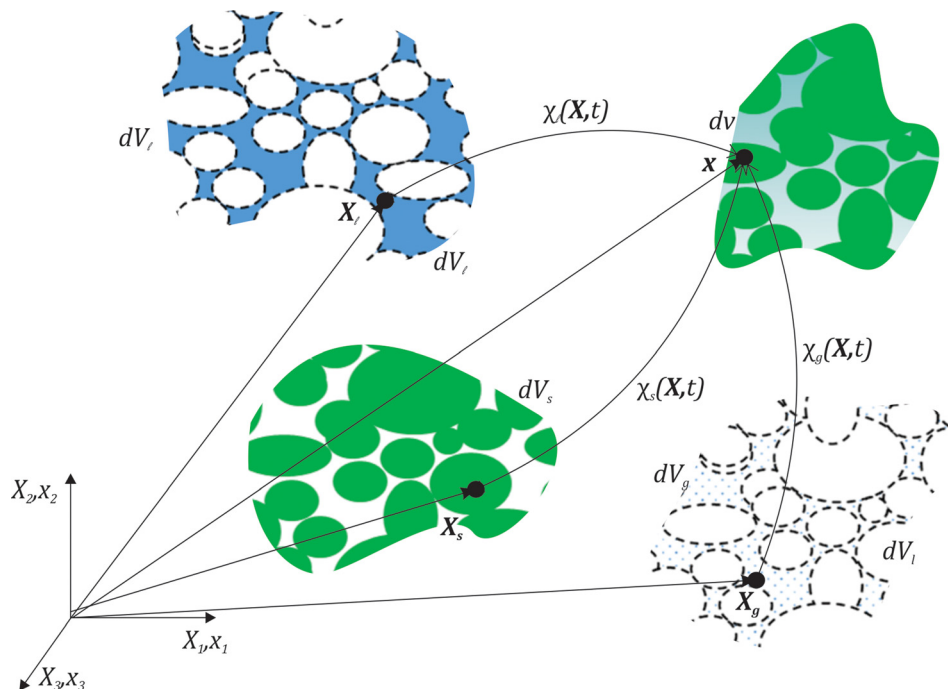


Fig. 1 A depiction of the deformation of each phase from its initial differential volume, dV_{α} , in their respective reference configurations to the final smeared differential volume, dv , in the final current configuration

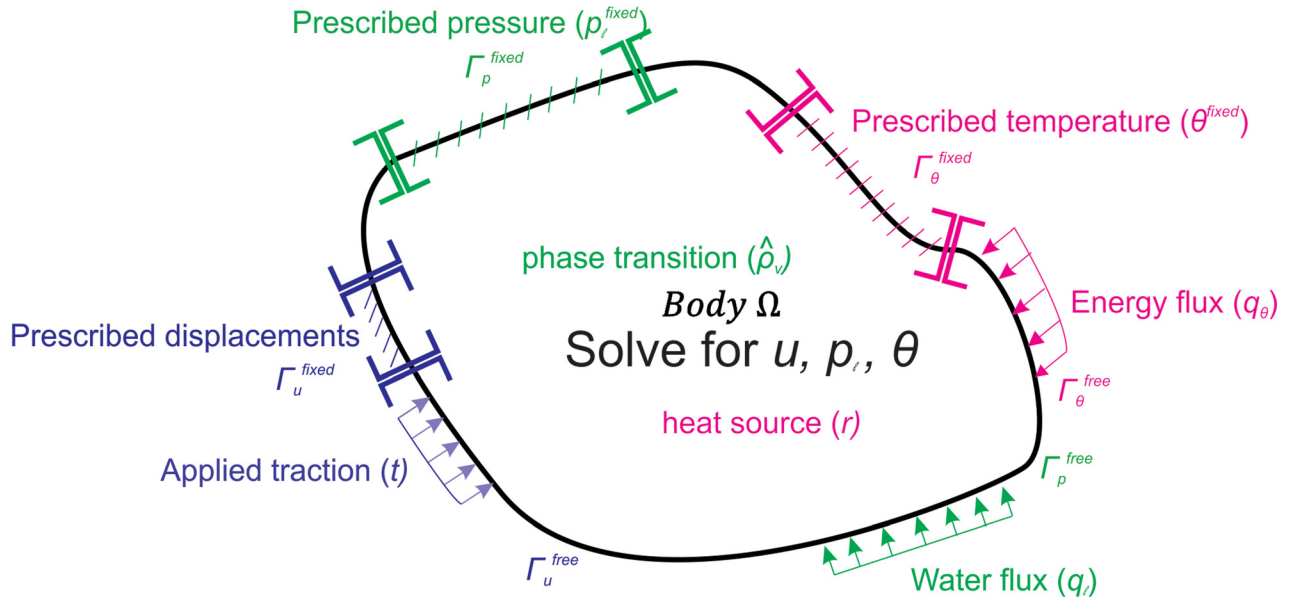


Fig. 2 Depiction of the problem setup for the balance equations where u , p_ℓ , and θ are the desired field variables. Fluxes and prescribed boundary conditions act on surfaces (Γ), while heat source (r) and phase transition ($\hat{\rho}^v$) act throughout the body (Ω).

variables, in this paper the desired field variables are the solid phase displacement, u , the liquid pore pressure, p_ℓ , and the average temperature of the smeared mixture, θ . In geomechanics, it is traditional to split the gas mixture into a combination of dry air and water vapor adding an additional balance of mass equation to solve for gas pressure [16]. However, in this paper, it is assumed that no dry air exists in the biological tissue and all gas is water vapor. Therefore, gas (vapor) pressure can be solved directly from the Clausius–Clapeyron equation as demonstrated later.

Figure 2 illustrates the problem setup including generalized boundary conditions, which include for the solid ECM—prescribed displacements, u^{fixed} , and applied traction, t , for the water species—prescribed liquid pore pressure, p_ℓ^{fixed} and flux, q_ℓ , in the form of vapor or liquid, and for energy—prescribed temperature, θ^{fixed} and energy flux, q_θ .

2.4 Balance of Mass. The balance of mass of the α phase for a total differential volume element, dv , can be written as

$$\frac{D^\alpha m_\alpha}{Dt} = \frac{D^\alpha}{Dt} \int_\Omega \rho^\alpha dv = \int_\Omega \hat{\rho}^\alpha dv \quad (13)$$

where $(D^\alpha(m_\alpha)/Dt)$ is the material time derivative of mass with respect to the α phase, and $\hat{\rho}^\alpha$ is the mass supply term [17]. It is assumed that the solid matrix cannot gain or lose mass ($\hat{\rho}^s = 0$), and that the water can change from liquid to vapor or vice versa, but that no water is added or lost

$$\hat{\rho}^g = -\hat{\rho}^\ell = \hat{\rho}^v \quad (14)$$

Applying these assumptions, localizing the integral, and applying Eq. (6), the balance of mass for each phase is

$$\frac{D^s n^s}{Dt} + n^s \text{div} v_s = 0 \quad (15)$$

$$\frac{D^\ell n^\ell}{Dt} + n^\ell \text{div} v_\ell = -\frac{\hat{\rho}^v}{\rho^{\ell R}} \quad (16)$$

$$\frac{D^g n^g}{Dt} + n^g \text{div} v_g = \frac{\hat{\rho}^v}{\rho^{gR}} \quad (17)$$

where $\text{div} v_\alpha$ is the divergence of the velocity, v_α , of the α phase, and $\hat{\rho}^v$ is the change in water mass due to vaporization or condensation. Assuming that the solid and liquid phases are incompressible, but allowing for density change due to temperature [18] and treating gas as ideal, the balance of mass equations become

$$\frac{D^s n^s}{Dt} + n^s \text{div} v_s - \beta_s^\theta n^s \frac{D^s \theta}{Dt} = 0 \quad (18)$$

$$\frac{D^\ell n^\ell}{Dt} + n^\ell \text{div} v_\ell - \beta_\ell^\theta n^\ell \frac{D^\ell \theta}{Dt} = -\frac{\hat{\rho}^v}{\rho^{\ell R}} \quad (19)$$

$$\frac{D^g n^g}{Dt} + n^g \text{div} v_g + \frac{1}{p_g} \frac{D^g p_g}{Dt} - \frac{1}{\theta} \frac{D^g \theta}{Dt} = \frac{\hat{\rho}^v}{\rho^{gR}} \quad (20)$$

A Lagrangian formulation is used for the FE formulation, such that all material time derivatives must be put in terms of the solid phase (i.e., the FE mesh will follow the solid ECM motion). Additionally, it is beneficial to combine Eqs. (18)–(20) with Eq. (7) into a single balance of mass equation for the mixture

$$\begin{aligned} & (\rho^{\ell R} S_\ell + \rho^{gR} S_g) \text{div} v_s - \left[(1-n) (\rho^{\ell R} S_\ell + \rho^{gR} S_g) \beta_s^\theta + n \rho^{\ell R} \beta_\ell^\theta \right] \\ & \times \frac{D^s \theta}{Dt} + n (\rho^{\ell R} - \rho^{gR}) \frac{D^s S_\ell}{Dt} + n S_g \frac{D^s \rho^{gR}}{Dt} \\ & + \text{div} (\rho^{gR} \tilde{v}_g^D + \rho^{\ell R} \tilde{v}_\ell^D) = 0 \end{aligned} \quad (21)$$

where \tilde{v}_f^D is the Darcy velocity of the fluid ($f = g$ or ℓ) phase, where $\tilde{v}_f^D = n^f (v_f - v_s)$.

2.5 Balance of Linear Momentum. According to de Boer [15], Holzapfel [17], and Coussy [19], the balance of linear momentum for the α phase can be written as

$$\begin{aligned} & \int_\Omega \left[v_\alpha \frac{D^\alpha \rho^\alpha}{Dt} + \rho^\alpha a_\alpha + \rho^\alpha \text{div} v_\alpha \right] dv \\ & = \int_\Omega (\rho^\alpha + b^\alpha + \hat{h}^\alpha) dv + \int_\Gamma t^\alpha da \end{aligned} \quad (22)$$

where \mathbf{t}^α is the traction acting on surface Γ , \mathbf{a}_α is the acceleration, \mathbf{b}^α is the body force, and $\hat{\mathbf{h}}^\alpha$ is the drag body force of all other phases acting on the α phase such that

$$\sum_{\alpha=s,\ell,g} \hat{\mathbf{h}}^\alpha = 0 \quad (23)$$

Localizing and applying Cauchy's theorem, Eq. (22) can be written as

$$\mathbf{v}_\alpha \frac{D^\alpha \rho^\alpha}{Dt} + \rho^\alpha \mathbf{a}_\alpha + \rho^\alpha \operatorname{div} \mathbf{v}_\alpha = \rho^\alpha \mathbf{b}^\alpha + \hat{\mathbf{h}}^\alpha + \operatorname{div} \boldsymbol{\sigma}^\alpha \quad (24)$$

where $\boldsymbol{\sigma}^\alpha$ is the partial Cauchy stress in the α phase. Summing over all phases, neglecting inertia terms, and applying Eq. (24), the total mixture balance of linear momentum is

$$\mathbf{0} = \rho^{\text{eff}} \mathbf{b} + \operatorname{div} \boldsymbol{\sigma} \quad (25)$$

where

$$\rho^{\text{eff}} = (1-n)\rho^s + n(S_\ell \rho^{\ell R} + S_g \rho^{gR}) \quad (26)$$

$$\mathbf{b}^\alpha = \mathbf{b} \quad (27)$$

The total Cauchy stress of the mixture, $\boldsymbol{\sigma}$, is defined by the effective stress principle as

$$\boldsymbol{\sigma} = \boldsymbol{\sigma}' - (\chi p_\ell + (1-\chi)p_g)\mathbf{1} \quad (28)$$

where $\boldsymbol{\sigma}'$ is the effective stress of the solid ECM, p_ℓ and p_g are the pore pressure of each fluid phase, and χ is the effective stress parameter representing the portion of the stress taken by the liquid and gas phases [18].

2.6 Balance of Energy. The first law of thermodynamics provides the balance of energy for the mixture, which for the α phase can be written as

$$\dot{E}^\alpha + \dot{K}^\alpha = P^\alpha + \dot{Q}^\alpha + \int_\Omega \hat{e}^\alpha dv \quad (29)$$

with

$$\dot{E}^\alpha + \dot{K}^\alpha = \int_\Omega \left[\hat{\rho}^\alpha \left(\frac{\mathbf{v}_\alpha \cdot \mathbf{v}_\alpha}{2} + e^\alpha \right) + \rho^\alpha \frac{D^\alpha e^\alpha}{Dt} \right] dv \quad (30)$$

$$P^\alpha = \int_\Omega \left[\boldsymbol{\sigma}^\alpha : \frac{D^\alpha \boldsymbol{\epsilon}^\alpha}{Dt} - \hat{\mathbf{h}}^\alpha \cdot \mathbf{v}_\alpha \right] da \quad (31)$$

$$\dot{Q}^\alpha = \int_\Omega [\rho^\alpha \dot{\gamma}^\alpha - \operatorname{div} \mathbf{q}_0^\alpha] dv \quad (32)$$

The material time derivatives following the α phase of internal energy, \dot{E}^α , and kinetic energy, \dot{K}^α , are a function of the partial mass density, ρ^α , the source or sink of mass density, $\hat{\rho}^\alpha$, the velocity, \mathbf{v}_α , and the internal energy, e^α , of the α phase. The rate of heat transfer to the α constituent, \dot{Q}^α , is dependent on both an energy supply source, $\dot{\gamma}^\alpha$, and the heat flux, \mathbf{q}_0^α , to each phase. P^α is the power imparted on the α phase and consists of a mechanical work term, $\boldsymbol{\sigma}^\alpha : (D^\alpha \boldsymbol{\epsilon}^\alpha / Dt)$, and the interphase momentum term, $\hat{\mathbf{h}}^\alpha \cdot \mathbf{v}_\alpha$, where $\boldsymbol{\epsilon}^\alpha$ is the small strain tensor of the α phase (here, we begin to assume small deformation theory). Finally, \hat{e}^α is the energy supply rate of the α constituent from all other constituents. Localizing and summing over all constituents, Eq. (29) becomes

$$\sum_{\alpha=s,\ell,g} \boldsymbol{\sigma}^\alpha : \frac{D^\alpha \boldsymbol{\epsilon}^\alpha}{Dt} + \hat{\mathbf{h}}^\alpha \cdot \mathbf{v}_\alpha - \rho^\alpha \frac{\mathbf{v}_\alpha \cdot \mathbf{v}_\alpha}{2} + \rho^\alpha \frac{D^\alpha e^\alpha}{Dt} - \rho^\alpha \dot{\gamma}^\alpha + e^\alpha \hat{\rho}^\alpha = 0 \quad (33)$$

2.7 Closure of Theory. Although the balance equations provide the backbone of TPM, additional equations, often called constitutive equations, are needed to reach a closed theory. In this work, several equations will be used to close the theory.

The second law of thermodynamics is used to motivate constitutive forms and can be written in the local form for the α constituent as

$$\hat{\rho}^\alpha \theta^\alpha \dot{\eta}^\alpha - \rho^\alpha \dot{\gamma}^\alpha + \rho^\alpha \theta^\alpha \frac{D^\alpha \eta^\alpha}{Dt} + \operatorname{div} \mathbf{q}_0^\alpha - \mathbf{q}_0^\alpha \cdot \frac{\operatorname{grad} \theta^\alpha}{\theta} \geq 0 \quad (34)$$

where η^α is the entropy per unit mass of the α phase. The Gibb's free energy per unit mass, g^f , of a fluid ($f = \ell, g$) phase is defined as

$$g^f = e^f - \frac{p^f}{\rho^f R} - \theta^f \eta^f \quad (35)$$

Taking the material time derivative with respect to f of Eq. (35), substituting it into Eq. (34) and combining with Eqs. (13) and (33) yield the entropy inequality of a fluid phase

$$\sum_{f=\ell,g} \rho^f \frac{\mathbf{v}_f \cdot \mathbf{v}_f}{2} - \hat{\mathbf{h}}^\alpha \cdot \mathbf{v}_f + \dot{e}^f - \rho^f \frac{\partial g^f}{\partial p^f} \frac{D^f p^f}{Dt} - \rho^f \frac{\partial g^f}{\partial \theta^f} \frac{D^f \theta^f}{Dt} - \rho^f \eta^f \frac{D^f \theta^f}{Dt} + n^f \frac{D^f p^f}{Dt} + p^f \frac{D^f n^f}{Dt} - \frac{\mathbf{q}_0^f \cdot \operatorname{grad} \theta^f}{\theta^f} \geq 0 \quad (36)$$

Defining the Helmholtz free energy per unit mass of the solid phase as

$$\psi^s = e^s - \theta^s \eta^s \quad (37)$$

and combining it with Eqs. (28), (33), and (34), the entropy inequality for the solid is

$$\boldsymbol{\sigma}' : \frac{D^s \boldsymbol{\epsilon}^{\text{skel}}}{Dt} + \left[(n^\ell - \chi) + (n^g - (1-\chi))p_g \right] \operatorname{div} \mathbf{v}_s - \hat{\mathbf{h}}^s \cdot \mathbf{v}_s + \dot{e}^s - \rho^s \eta^s \frac{D^s \theta^s}{Dt} - \rho^s \frac{D^s \psi^s}{Dt} - \frac{\mathbf{q}_0^s \cdot \operatorname{grad} \theta^s}{\theta^s} \geq 0 \quad (38)$$

where the strain tensor of the solid phase is the same as that of the solid ECM, e.g., $\boldsymbol{\epsilon}^{\text{skel}} = \boldsymbol{\epsilon}^s$. Following the procedure outlined by de Boer [15], Coussy [19], and Wang [20], through combining Eqs. (21), (36), and (38), the entropy inequality for the mixture can be written as

$$\begin{aligned} & \frac{1}{2} \hat{\rho}^\ell \mathbf{v}_\ell \cdot \mathbf{v}_\ell + \frac{1}{2} \hat{\rho}^g \mathbf{v}_g \cdot \mathbf{v}_g - \hat{\rho}^\ell \mathbf{v}_\ell \cdot \tilde{\mathbf{v}}_\ell - \hat{\rho}^g \mathbf{v}_g \cdot \tilde{\mathbf{v}}_g \\ & + \left\{ [n^g - (1-\chi)]p_g - (n^\ell - \chi)p_\ell \right\} \beta_s^\theta - \rho^s \eta^s - \rho^s \frac{\partial \psi^s}{\partial \theta} \\ & \times \frac{D^s \theta^s}{Dt} + \rho^\ell \left[\frac{\partial g^\ell}{\partial \theta^\ell} - \eta^\ell \right] \frac{D^\ell \theta^\ell}{Dt} + \rho^g \left[\frac{\partial g^g}{\partial \theta^g} - \eta^g \right] \frac{D^g \theta^g}{Dt} \\ & - \left[\rho^s \frac{\partial \psi^s}{\partial S_\ell} + n^s \right] \frac{D^s S_\ell}{Dt} + \left[n^\ell - \rho^\ell \frac{\partial g^\ell}{\partial p^\ell} \right] \frac{D^\ell p_\ell}{Dt} \\ & + \left[n^g - \rho^g \frac{\partial g^g}{\partial p^g} \right] \frac{D^g p_g}{Dt} - \tilde{\mathbf{v}}_\ell^D \cdot [\operatorname{grad} p_\ell - \rho^{\ell R} \mathbf{b}^\ell] \\ & - \tilde{\mathbf{v}}_g^D \cdot [\operatorname{grad} p_g - \rho^{gR} \mathbf{b}^g] + \left(\boldsymbol{\sigma}' - \frac{\rho^s \partial \psi^s}{\partial \boldsymbol{\epsilon}^{\text{skel}}} \right) : \frac{D^s \boldsymbol{\epsilon}^{\text{skel}}}{Dt} \\ & - \frac{1}{\theta} \mathbf{q}_0 \cdot \operatorname{grad} \theta \geq 0 \end{aligned} \quad (39)$$

where $\tilde{\mathbf{v}}_f = \mathbf{v}_f - \mathbf{v}_s$ and \mathbf{q}_0 is the heat flux. Using arguments by Coleman and Noll [21] and Coussy [19] that $D^s \boldsymbol{\epsilon}^{\text{skel}} / Dt$, $D^f p^f / Dt$, $D^s S_\ell / Dt$, and $D^2 \theta^\alpha / Dt$ are independent processes that can be varied separately, it is then required that

$$\left\{ [n^s - (1 - \chi)]p_g - (n^\ell - \chi)p_\ell \right\} \beta_s^\theta - \rho^s \eta^s - \rho^s \frac{\partial \psi^s}{\partial \theta} = 0 \quad (40)$$

$$\left[\frac{\partial g^f}{\partial \theta^f} - \eta^f \right] = 0, \text{ for } f = g, \ell \quad (41)$$

$$\left[\rho^s \frac{\partial \psi^s}{\partial S_\ell} + ns \right] = 0, \text{ for } f = g, \ell \quad (42)$$

$$\left(\boldsymbol{\sigma}^f - \frac{\rho^s \partial \psi^s}{\partial \boldsymbol{\epsilon}^{skel}} \right) = \mathbf{0}, \quad (43)$$

$$-\tilde{\mathbf{v}}_f^D \cdot [\text{grad} p_f - \rho^{fR} \mathbf{b}^f] \geq 0 \quad (44)$$

$$-\frac{1}{\theta} \mathbf{q}_\theta \cdot \text{grad} \theta \geq 0 \quad (45)$$

Therefore, to remain thermodynamically consistent, the constitutive models for the mixture must meet the following requirements:

$$\rho^s \eta^s = \left\{ [n^s - (1 - \chi)]p_g - (n^\ell - \chi)p_\ell \right\} \beta_s^\theta - \rho^s \frac{\partial \psi^s}{\partial \theta} \quad (46)$$

$$ns = -\rho^s \frac{\partial \psi^s}{\partial S_\ell} \quad (47)$$

$$\eta^f = \frac{\partial g^f}{\partial \theta^f} \text{ for } f = \ell, g \quad (48)$$

$$\frac{n^f}{\rho^f} = \frac{\partial g^f}{\partial p_f} \text{ for } f = \ell, g \quad (49)$$

$$\boldsymbol{\sigma}^f = \rho^s \frac{\partial \psi^s}{\partial \boldsymbol{\epsilon}^{skel}} \quad (50)$$

Applying the conclusion shown in Eqs. (44)–(49), assuming the temperature of each phase at a point is the same, e.g.,

$$\theta = \theta^\alpha \text{ for } \alpha = s, \ell, g \quad (51)$$

combining them with Eqs. (35) and (37) and simplifying yield the balance of energy equations of the combined mixture

$$\begin{aligned} & \rho^\ell \theta \frac{D^\ell \eta^\ell}{Dt} + \rho^g \theta \frac{D^g \eta^g}{Dt} + \rho^s \theta \frac{D^s \eta^s}{Dt} + \tilde{\mathbf{v}}_\ell^D \cdot [\text{grad} p_\ell - \rho^{\ell R} \mathbf{b}^\ell] \\ & + \tilde{\mathbf{v}}_g^D \cdot [\text{grad} p_g - \rho^{gR} \mathbf{b}^g] - \frac{1}{2} \hat{\rho}^\ell \mathbf{v}_\ell \cdot \mathbf{v}_\ell - \frac{1}{2} \hat{\rho}^g \mathbf{v}_g \cdot \mathbf{v}_g \\ & + \hat{\rho}^\ell \mathbf{v}_\ell \cdot \tilde{\mathbf{v}}_\ell + \hat{\rho}^g \mathbf{v}_g \cdot \tilde{\mathbf{v}}_g - \rho^\ell \dot{\chi}^\ell - \rho^g \dot{\chi}^g - \rho^s \dot{\chi}^s + \text{grad} \mathbf{q}_\theta^\ell \\ & + \text{grad} \mathbf{q}_\theta^g + \text{grad} \mathbf{q}_\theta^s + \hat{\rho}^v H_{\text{vap}} = 0 \end{aligned} \quad (52)$$

Combining the heat sink and flux terms, neglecting body forces, moving material time derivatives to be in reference to the solid phase, and introducing the definition of specific heat, C_p^α , as

$$\rho^\alpha C_p^\alpha \frac{D^\alpha \theta^\alpha}{Dt} = \rho^\alpha \theta^\alpha \frac{D^\alpha \eta^\alpha}{Dt} \quad (53)$$

allow the final balance of energy to be written as

$$\begin{aligned} & (\rho C_p)_{\text{eff}} \frac{D^s \theta}{Dt} + \rho^{\ell R} C_p^\ell \tilde{\mathbf{v}}_\ell^D \cdot \text{grad} \theta + \rho^{gR} C_p^g \cdot \text{grad} \theta - \rho \dot{\chi} \\ & + \text{grad} \mathbf{q}_\theta + \hat{\rho}^v H_{\text{vap}} - \hat{\rho}^\ell \frac{\mathbf{v}_\ell \cdot \mathbf{v}_\ell}{2} - \hat{\rho}^g \frac{\mathbf{v}_g \cdot \mathbf{v}_g}{2} - \hat{\rho}^v \mathbf{v}_\ell \cdot \tilde{\mathbf{v}}_\ell \\ & + \hat{\rho}^v \mathbf{v}_g \cdot \tilde{\mathbf{v}}_g + \tilde{\mathbf{v}}_\ell^D \cdot \text{grad} p_\ell + \tilde{\mathbf{v}}_g^D \cdot \text{grad} p_g = 0 \end{aligned} \quad (54)$$

where the effective specific heat, $(\rho C_p)_{\text{eff}}$, is defined as

$$(\rho C_p)_{\text{eff}} = \rho^s C_p^s (1 - n) + n [S_\ell \rho^\ell C_p^\ell + S_g \rho^g C_p^g] \quad (55)$$

the total heat flux, \mathbf{q}_θ , is

$$\mathbf{q}_\theta = \mathbf{q}_\theta^s + \mathbf{q}_\theta^\ell + \mathbf{q}_\theta^g \quad (56)$$

and the total heat source per unit mass, $\dot{\chi}$, is

$$\dot{\chi} = \dot{\chi}^s + \dot{\chi}^\ell + \dot{\chi}^g \quad (57)$$

Additionally, the heat flux is assumed to be isotropic and, therefore, can be defined as

$$\mathbf{q}_\theta = k_t^{\text{eff}} \text{grad} \theta \quad (58)$$

where k_t^{eff} is the total thermal conductivity of the mixture defined as

$$k_t^{\text{eff}} = (1 - n)k_t^s + n(S_\ell k_t^\ell + S_g k_t^g) \quad (59)$$

where k_t^α is the thermal conductivity of the α phase. Furthermore, it is assumed that water vapor reaches its saturation pressure [22]. Therefore, the Clausius–Clapeyron equation can be used to calculate gas pressure, p_g

$$p_g = p_{g,s0} \exp\left(-\frac{M_m H_{\text{vap}}}{R} \left[\frac{1}{\theta} - \frac{1}{\theta_0}\right]\right) \quad (60)$$

where M_m is the molar mass of the vapor, H_{vap} is the latent heat of vaporization, R is the ideal gas constant, and $p_{g,s0}$ is the saturated gas pressure at reference temperature, θ_0 . Using this calculated gas pressure, the van Genuchten (Eq. (61)) equation can now be used to relate the liquid saturation with the capillary pressure [15,23], s , which is the difference between the liquid and gas pressures

$$S_e = \frac{S_\ell - S_r}{S_s - S_r} = \left(\frac{1}{1 + \left(\frac{s}{a}\right)^{n_g}} \right)^m \quad (61)$$

$$m = 1 - \frac{1}{n} \quad (62)$$

$$s = p_g - p_\ell \quad (63)$$

where, S_e is the effective degree of saturation, S_r is the residual degree of saturation, and S_s is the saturated degree of saturation, taken to be 1. Literature fails to provide values for constants a , n_g , m , and S_r for biological tissue, forcing the authors to look to fields such as food processing [24] and geomechanics [16] for

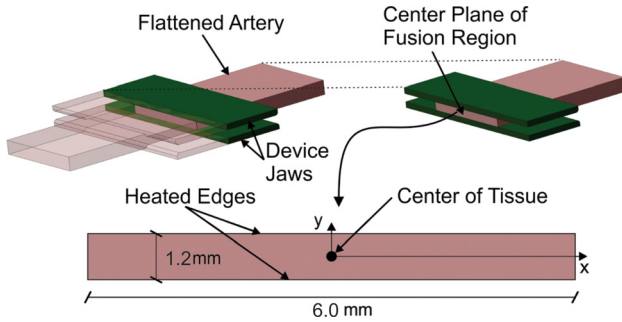


Fig. 3 Depiction of the tissue clamped within the Commed Altrus® jaws and the two-dimensional plane to be simulated

values. Additionally, Darcy's law will provide the relative velocities of the fluids [16] (the body force term is neglected)

$$\vec{v}_f^D = -\frac{k_{rel}^f k_{int}^f}{\mu^f} \text{grad} p_f \quad (64)$$

where μ^f is the viscosity of the fluid phase f . The relative permeability of each fluid, k_{rel}^f , includes the Kozeny–Carman relationship and is defined as

$$k_{rel}^f = \frac{(n^f)^3}{1 - (n^f)^2} \frac{1 - (n_0^f)^2}{(n_0^f)^3} \quad (65)$$

where n^f and n_0^f are the current and initial volume fraction of each fluid phase, and the intrinsic permeability, k_{int}^f , is defined as

$$k_{int} = k_{0int} \gamma(S_\ell)$$

where k_{0int} is a material constant, and $\gamma(S_\ell)$ is a saturation-dependent parameter defined for the liquid phase as

$$\gamma(S_\ell) = \begin{cases} \left(\frac{S_\ell - S_r}{1 - S_r}\right)^3 & S_\ell > S_r \\ 0 & S_\ell < S_r \end{cases} \quad (66)$$

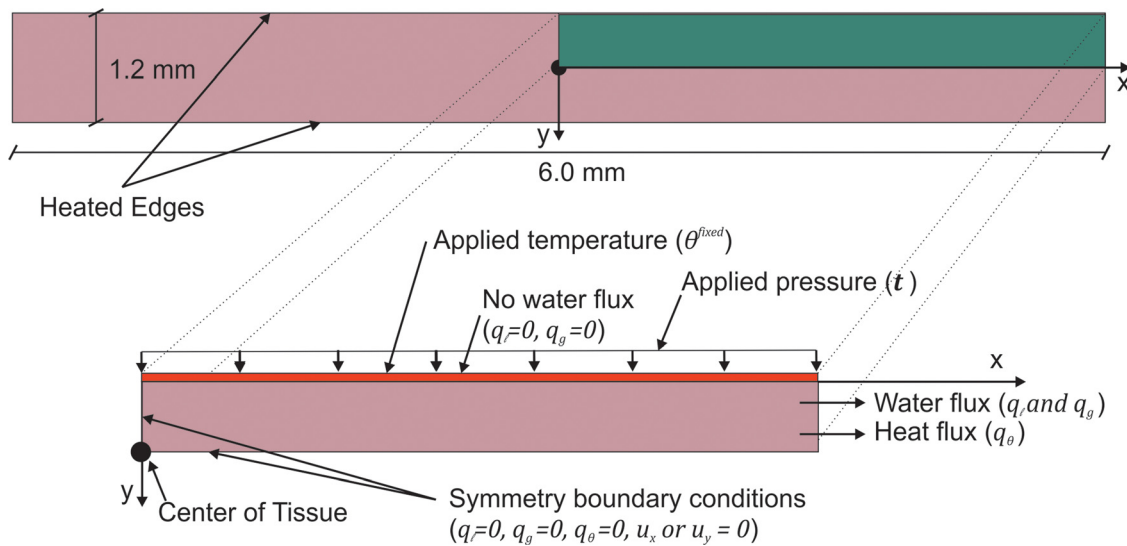


Fig. 4 Depiction of the quarter-symmetry section of tissue and applied boundary conditions. The device jaws apply temperature and pressure to the top. Symmetry boundary conditions are applied to the bottom and left edges. Heat and water are allowed to flow through the right edge.

and for the gas phase as

$$\gamma(S_g) = \begin{cases} 1 - 1.1S_g & S_g < 1/1.1 \\ 0 & S_g > 1/1.1 \end{cases} \quad (67)$$

where S_r is the residual degree of saturation, S_ℓ is the degree of liquid saturation, and S_g the gaseous degree of saturation defined as $S_g = 1 - S_\ell$ [25]. These equations assume that as the liquid saturation (S_ℓ) approaches the residual saturation (S_r), it becomes increasingly difficult for the fluids to flow through the tissue.

Finally, the solid ECM is assumed to be elastic; thus, the effective ECM stress, σ' , can be represented by

$$\sigma' = C \epsilon^{\text{skel}} \quad (68)$$

where C is the isotropic elasticity tensor that meets the thermodynamic requirements set forth in Eq. (43), and ϵ^{skel} is the small strain within the solid ECM. This paper examines three different constitutive equations: a simple linear elastic, a bilinear elastic, and an exponential elastic equation to determine the elasticity tensor, C .

2.8 FE Implementation. As stated earlier, the field variables to be solved using the finite element method are pore liquid pressure, p_ℓ , the smeared temperature, θ , and the solid ECM displacement vector, \mathbf{u} . The balance of mass, linear momentum, and energy equations (Eqs. (21), (25), and (54)) were put into weak form and linearized with respect to the desired variables. To avoid element locking, isoparametric quadrilateral elements biquadratic in displacement and bilinear in temperature and pore pressure were used. A standard backward Euler time-stepping scheme was implemented with Newton–Raphson iterations to obtain convergence during each time step. All calculations were conducted using a custom written code in MATLAB 2015b. To handle the highly nonlinear nature of this problem efficiently, an adaptive time-stepping scheme was performed by altering the time-step size based on the number of Newton–Raphson iterations needed for convergence during the previous step. The FE code was rigorously verified through comparison with published TPM FE results in the geomechanics field [16,20] and by comparing portions of the code with simulations conducted using the commercial software Comsol Multiphysics®.

Table 1 Material properties, initial conditions, and boundary conditions

	Material property	Value	Description	Source
Universal constants	R	8.314 N·m/mol K	Ideal gas constant	[28]
	M_m	0.018 kg/mol	Molar mass of water	[28]
Solid skelton structure	E_{lin}	6.22 MPa	Linear elastic Young's modulus	Measured
	E_1	2.0 MPa	Bilinear elastic Young's modulus 1	Measured
	E_2	10.12 MPa	Bilinear elastic Young's modulus 2	Measured
	E_{exp}	4.62 MPa	Exponential elastic Young's modulus	Measured
	ν^{skel}	0.3	Poisson's ratio	[29]
Thermal constants	α_s	$2.5 \times 10^{-4} \text{ K}^{-1}$	Solid thermal expansion coefficient	[30]
	β_s^0	$3^* \alpha_s$	Solid volumetric thermal expansion coefficient	N/A
	β_ℓ^0	$4.0 \times 10^{-4} \text{ K}^{-1}$	Water volumetric thermal exp. coefficient	[31]
	C_p^s	145.83 J/(kg K)	Specific heat of solid	[26]
	C_p^ℓ	4179 J/(kg K)	Specific heat of liquid water	[28]
	C_p^g	1850 J/(kg K)	Specific heat of water vapor	[28]
	k_t^s	0.5 W/(m K)	Thermal conductivity of solid	[26]
	k_t^ℓ	0.6 W/(m K)	Thermal conductivity of liquid water	[28]
	k_t^g	0.025 W/(m K)	Thermal conductivity of water vapor	[28]
	H_{vap}	$2.264 \times 10^6 \text{ J/kg}$	Latent heat of vaporization of water	[28]
	h_t	25 W/(m ² K)	Convective heat transfer coefficient	[32]
	θ_{amb}	25 °C = 298 K	Ambient temperature	N/A
	Densities	ρ^{sR}	1050 (kg/m ³)	Real density of solid
$\rho^{\ell R}$		$1000/(1 + 4 \beta_\ell^0 \theta)$	Real density of water	[28]
ρ^{gR}		Ideal gas		N/A
Mass transport constants	$k_{o,int}^\ell$	$5 \times 10^{-14} \text{ m}^2$	Intrinsic permeability of liquid water	[24]
	$k_{o,rel}^\ell$	Eq. (61)	Relative permeability of water	[15]
	k_{int}^g	$10 \times 10^{-14} \text{ m}^2$	Intrinsic permeability of water vapor	[24]
	k_{int}^s	Eq. (61)	Relative permeability of water	[15]
	μ_ℓ	$5.5 \times 10^{-4} \text{ Pa}\cdot\text{s}$	Viscosity of liquid water	[24]
	μ_g	$1.8 \times 10^{-5} \text{ Pa}\cdot\text{s}$	Viscosity of water Vapor	[24]
	n_{vg}	1.6, 1.8, 2.0	Constant for Clausius–Clapeyron	[16], N/A
	a	$19.4 \times 10^3 \text{ Pa}$	Constant for Clausius–Clapeyron	[16]
	S_r	0.25, 0.3, 0.35	Constant for Clausius–Clapeyron	[16], N/A
	h_m	0.0015 m/s	Convective mass transfer coefficient	[24]
	ρ_{amb}	0.073 kg/m ³	Ambient water vapor density	Ideal gas
	p_{amb}	$1.01 \times 10^5 \text{ Pa}$	Ambient pressure	N/A
	Initial conditions and model parameters	$p_{g,o}$	$1.01 \times 10^5 \text{ Pa}$	Initial water vapor pressure
n_o		0.78	Initial porosity	[26]
$p_{\ell,o}$		$1.01 \times 10^5 \text{ Pa}$	Initial liquid water pressure	N/A
θ_{amb}		37 °C = 310 K	Initial ambient temperature	Measured
$S_{\ell,o}$		0.99	Initial liquid water saturation	N/A
θ_{app}		$t \begin{cases} = \frac{t}{.5} * (\theta_{max} - 37) t < .5 \\ = \theta_{max}, t > .5 \end{cases}$	Applied temperature	Measured
θ_{max}		Varies	Maximum jaw temperature	N/A
t		$2.7 \times 10^6 \text{ Pa}$	Applied traction	Measured
T		5 s	Total time	N/A
dt_0		0.0001 (s)	Initial time step	N/A

2.9 Experimental Measurements. The experimental results used to evaluate the performance of the FE model were taken from data published within the literature [2,26,27] as well as supplemental experiments conducted by the first and third authors following the same procedures outlined in these papers. The temperature measurements were taken within the lumen of a compressed artery using an array of thermocouples. To find water content, a portion of tissue was fused and then weighed. It was then dried completely and weighed again. The percent weight of water is calculated from these measurements. Full experimental details for tissue temperature and water content measurement can be found in the works published by Cezo et al. [26,27].

To obtain the deformation of the tissue while loaded to 100 N during the tissue fusion process, a custom testing setup affixing Conmed Altrus[®] jaws, to a uniaxial material testing system (MTS; MTS Insight 2 Electromechanical Testing System), was used. The thickness of eight porcine artery sections was recorded via optical microscope, and then each arterial section was placed

between the Altrus[®] jaws, and a 100 N force was applied using a proportional–integral–derivative control algorithm. Once the 100 N force was reached, the heaters were activated for 3 s. The deformation in the y-direction of the tissue and the force were recorded throughout the loading and heating process. To obtain the Young's Modulus, E , used in the finite element simulations, a best fit analysis was conducted using the engineering stress and strain recorded in the tissue after mechanically loading the tissue, but before heating. A more detailed explanation of the MTS attachments and experimental setup can be found in the work by Fankell et al. [2].

2.10 Tissue Fusion Simulations. Now that the framework for a multiphase TPM FE model has been established, its use in simulating heated biological tissue, specifically thermal tissue fusion, will be demonstrated. Figures 3 and 4 show the quarter-symmetry, two-dimensional section representing the center of the

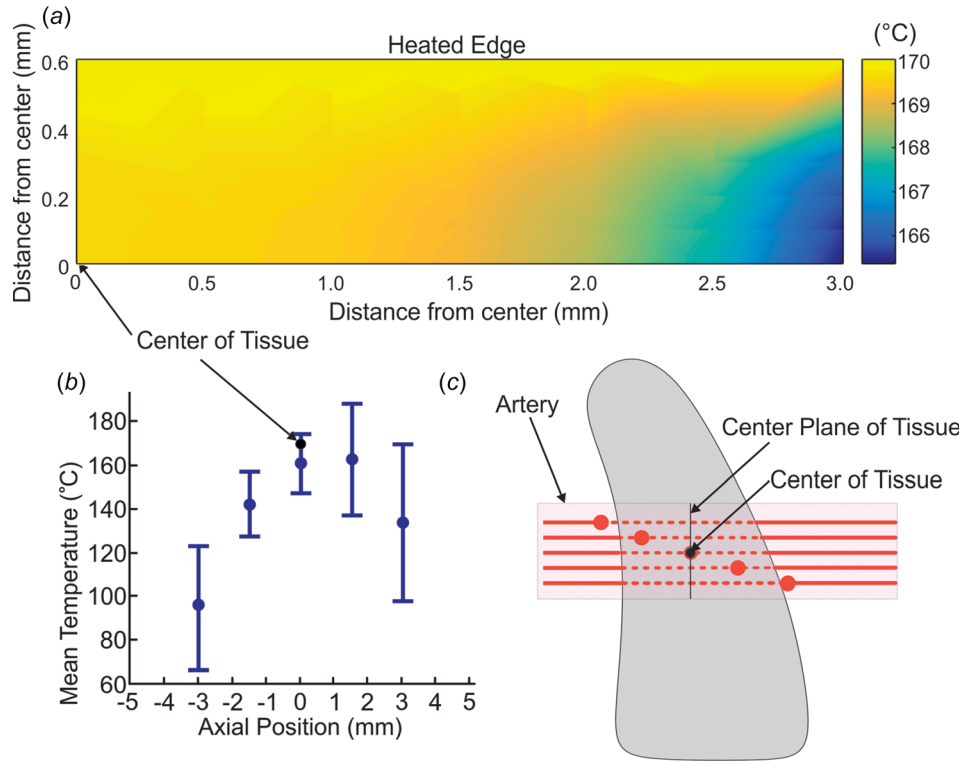


Fig. 5 (a) The temperature (°C) within the tissue for an applied 170°C and an $S_r = 0.3$ at the end of 5 s. (b) and (c) The temperature at the center of the tissue as it is compared to published experimental results [5]. Only one data point can be compared as all other experimental points are located too far from the center plane of the tissue.

tissue clamped within the jaws of a Conmed Altrus tissue fusion device used in the simulations and the applied boundary conditions.

2.11 Boundary Conditions. Three different temperature boundary conditions exist within the thermal tissue fusion FE model. The first is the symmetric boundary condition, which sets the heat flux, q_θ , through the surface equal to 0 (i.e., adiabatic)

$$q_\theta = q_\theta \cdot \mathbf{n} = 0 \text{ on } \Gamma_\theta^{\text{sym}} \quad (69)$$

The second thermal boundary condition is a prescribed temperature boundary condition representing the temperature of the jaws, θ^{fixed}

$$\theta(t) = \theta^{\text{fixed}}(t) \text{ on } \Gamma_\theta^{\text{fixed}} \quad (70)$$

Finally, on all free edges, free convection is expected to occur. Thus, the normal heat flux, q_θ , is specified as

$$q_\theta = h_t(\theta - \theta_{\text{amb}}) \text{ on } \Gamma_p^{\text{free}} \quad (71)$$

where h_t is the heat transfer coefficient, and θ_{amb} is the ambient temperature. Two water species boundary conditions are implemented. The first is an impermeable or symmetric boundary condition preventing flow through the boundary

$$q_\ell = q_g = 0 \quad (72)$$

The second boundary condition consists of the fluid flux, q_f , due to the difference of pore pressure across the boundary

$$q_f = -\frac{k_{\text{rel}}^f k_{\text{int}}^f}{\mu^f} \rho^{2R} S_f (p_f - p_{\text{amb}}) A \text{ for } f = l, g \text{ on } \Gamma_p^{\text{free}} \quad (73)$$

where p_{amb} is the ambient fluid pressure, and A is the boundary area. The last boundary conditions are an applied traction, \mathbf{t} , and a symmetric boundary condition fixing displacements

$$\mathbf{u} \cdot \mathbf{n} = 0 \text{ on } \Gamma_u^{\text{fixed}} \quad (74)$$

2.12 Material Properties. Material properties unable to be experimentally measured in the lab were obtained from several sources within the literature. If material properties specifically pertaining to the artery wall were unavailable, properties of tissue similar in composition to the artery wall were used. As it was not possible at this time to find values for the van Genuchten parameters, a parametric study of the parameters S_r and $n_{v,g}$ was conducted to determine the optimal parameters for matching experimental data. To determine the structural mechanical properties, E_{lin} , E_1 , E_2 , and E_{exp} , needed for the constitutive models, a nonlinear regression analysis using measured experimental stress-strain values was conducted using the commercial statistics software Minitab®. All material properties, initial condition, and boundary condition values along with the source they were found in are listed in Table 1.

2.13 Simulations. Seven different simulations were run attempting to predict experimental results of tissue displacement, water content, and internal tissue temperature. The maximum applied temperature, θ_{max} , varied from 120°C to 200°C, and simulations were run for 5 s (the same time period as the experiment). The simulation was conducted in three steps: (1) the applied traction matching that of the applied force seen in the experiments was applied during a 2 s step, (2) the temperature was applied during a 1 s step, and (3) the temperature held for 2 s.

Mesh sensitivity studies were conducted to find the most efficient simulation parameters. This was done by running a simulation, halving the mesh size, rerunning the simulation, and

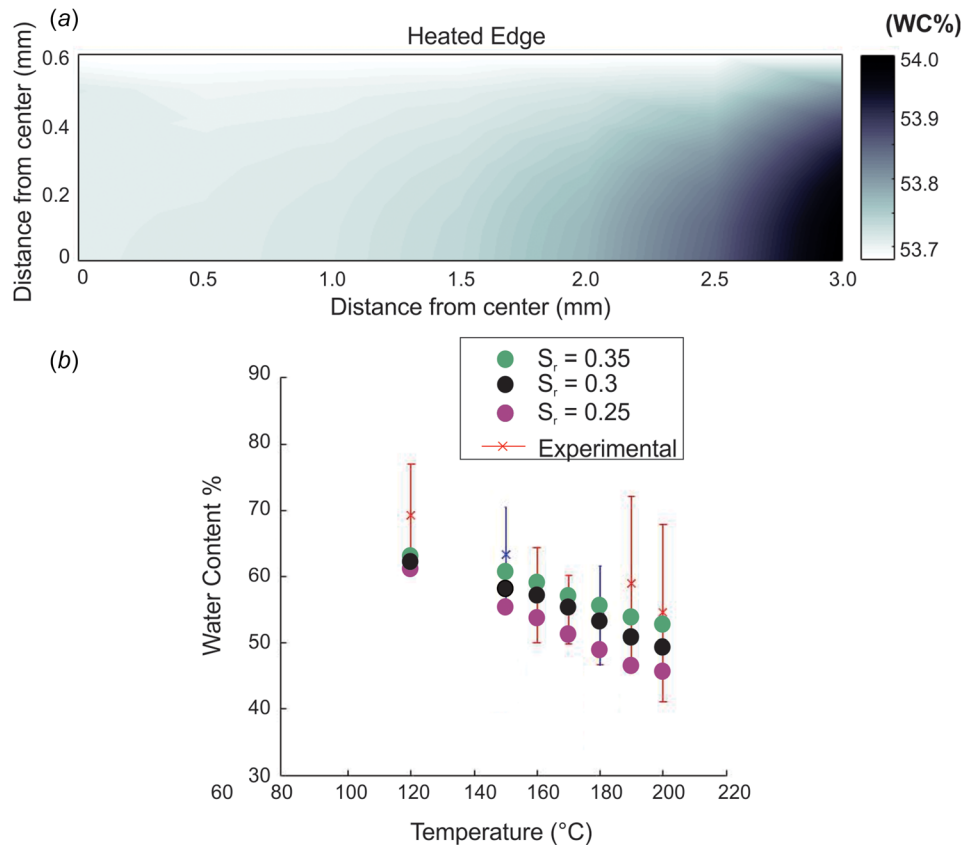


Fig. 6 (a) The water content at 5 s within the center plane of the tissue for a simulation applying 170 °C and an $S_r = 0.3$. (b) Dots representing the average water content within the tissue for applied temperatures of 120–200 °C for an S_r of 0.25, 0.30, and 0.35 are plotted against measured experimental results. All simulated results of water content fell within one standard deviation of the average experimental results with an S_r of 0.30 producing results nearest the mean of the experimental results. Note: Experimental results include Cezo's published results and supplemental results obtained following the same procedure ($T = 150\text{C}$ and $T = 180\text{C}$, $n = 12$).

comparing the solution vectors. This process was continued until the norm of the difference of the solution vectors was less than 1%. As high-temperature gradients and vaporization rates can occur during portions of the simulations, convergence often depended greatly on time-step size. Time-step size was determined by choosing an initial time step of 0.0001 s and recording the number of Newton–Raphson iterations required for convergence during the current time step. If this value was greater than or less than a certain threshold (seven iterations and two iterations, respectively), the time-step size was halved or doubled for the next step accordingly. Once the simulations were complete, the results were compared with experimental measurements.

3 Results

Figure 5 shows the temperature profile within the tissue at the end of a simulation ($\theta_{\max} = 170\text{ °C}$, $t_{\max} = 5\text{ s}$). The temperature at the tissue center is then compared to published results by Cezo et al. [27]. The results for the predicted temperature fall within one standard deviation of measured experimental results. The sensitivity analysis of the parameter, n_{vg} , showed less than a 1% difference in the solutions when changed by 20% (results not shown); however, the value selected for the residual degree of saturation parameter, S_r impacted the final predicted water content. Figure 6 shows the water content by weight throughout the tissue at the end of a simulation ($\theta_{\max} = 170\text{ °C}$, $t_{\max} = 5\text{ s}$) for S_r values of 0.25, 0.3, and 0.35. The water content falls within one standard deviation of the mean measured experimental results in each of the seven comparisons for all values of S_r and predicts

values closest to the measured experimental mean for an S_r of 0.3. Figure 7 compares experimentally measured stress–strain curves in the y-direction of the tissue to the simulated stress–strain curve of the tissue as the load is applied before heating. The experimental model using a linear elastic constitutive model deviates from the measured experimental results (mean standard error (MSE) of 0.33) for the majority of the curve, but ends at the same stress–strain point at the end of loading. The bilinear constitutive model and the exponential elastic models had a MSE of 0.21 and 0.18, respectively. The bilinear elastic simulation took an average of 1.1 times longer than the linear elastic simulation, whereas the simulation applying an exponential elastic material model took an average of 1.4 times as long as the simulation using a linear elastic material. Figure 8 displays the measured experimental and simulated vertical deformation against time before and during heating of the tissue. Before heating, the tissue deflects as expected for a fully saturated porous medium. During heating, the experimental results show an increase in downward deflection as the temperature increases. The simulation shows a decrease in downward deflection with temperature increase, and then an increase in deflection after a steady-state temperature is reached ($\sim 3\text{ s}$). Each simulation predicts a measured experimental deflection of within 15% throughout the simulation.

4 Discussion

This work provides a method for conducting TPM finite element simulations of biological tissue enabling one to evaluate the physics occurring within the tissue when loaded, thermally and/or

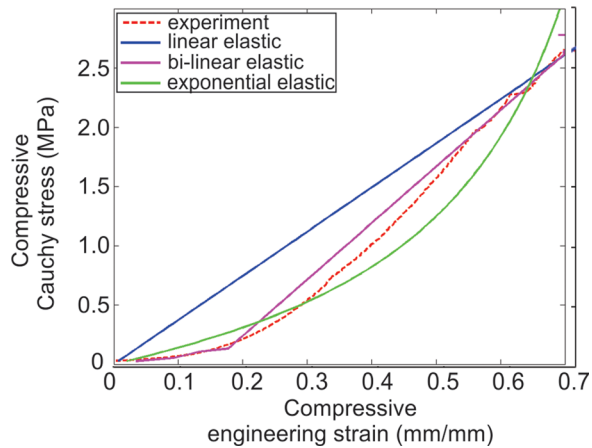


Fig. 7 The average recorded stress–strain curves for eight porcine splenic arteries (standard deviation of 0.12 MPa) compared to the simulated stress–strain curves of a linear elastic (MSE = 0.33), bilinear elastic (MSE = 0.21), and exponential elastic (MSE = 0.18) solid material model before heating

mechanically, by an external source. The model incorporates the fluid transport through the tissue, including phase change between liquid water and water vapor, the heat transfer through the tissue, and the deformation of the tissue. Using this method, the simulations of thermal tissue fusion were then conducted and compared to experimental results. The simulations were able to predict temperature and water content even though limited by small deformation theory.

4.1 Temperature. Figure 5 shows the simulated temperature at the end of an applied 170 °C temperature simulation. By this point (5 s), the simulation has reached steady-state, and the temperature at the center of the tissue is 169 °C which is 6 °C higher than the mean published experimental results [27], though still within a standard deviation of the results. This discrepancy is due to the assumption of perfect thermal conduction at the jaw edge. To better represent true device–tissue interaction, the conductivity between jaw edge and tissue edge needs to be taken into account. Even with the simplifying assumption of perfect conduction, the simulation predicts the center tissue temperature within one standard deviation of the measured experimental mean.

4.2 Water Content. Each of the seven simulations run for all values of the residual degree of saturation, S_r , predicted the average final water content within one standard deviation of the experimentally measured mean [26] with the value of $S_r = 0.3$ predicting final water content values closest to the mean measured experimental value. The value of residual saturation represents the amount of water left bound in the tissue that is impossible to be driven out via a tissue fusion device. Ideally, it would be beneficial to conduct separate experimental measurements to provide the specific van Genuchten parameters; however, these parameters prove particularly difficult to measure in biological tissue, and the measurement of them is currently left as future work. Thus, the sensitivity study presented here provides a baseline for researchers moving forward with this type of analysis.

4.3 Deformation. The deformation predicted by the three elastic constitutive models shown in Figs. 7 and 8 shows that although the final displacement before heating is accurately predicted, the model is limited by its linear elastic, small strain assumption. This is seen in Fig. 7 when the linear elastic stress–strain curve of the tissue deviates significantly from the measured stress–strain curve, and in Fig. 8 when the small deformation assumption limits the ability of all three models to predict

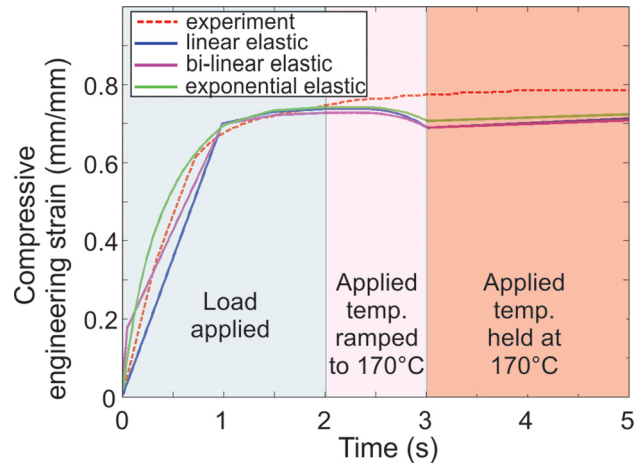


Fig. 8 The average measured engineering strain (standard deviation of 0.033) for the eight fused porcine arteries during mechanical loading (0–2 s), while heated up to an applied temperature of 170 °C (2–3 s) and at a constant applied temperature of 170 deg (4–5 s)

the tissue deflection as the tissue is heated. Despite these limitations, the model still accurately predicts the fluid and thermal transport occurring in the arterial tissue and estimates the final vertical deformation of the tissue to within 15% of the measured experimental mean. A more inclusive TPM FE model utilizing large deformation theory is needed for applications requiring more accurate analysis. While the small deformation theory may be limited, it is still a valuable tool for two reasons. First, simulations assuming small deformations will decrease simulation time significantly when compared to simulations utilizing full nonlinear large deformation theory. This is already seen in the comparison in computation time between the linear elastic and exponential elastic simulations and would be exacerbated if compared to full large deformation theory. This reduction in computational time would be valuable in applications where a real-time prediction of tissue deformation is desired, but exact accuracy is not necessary such as seen in the field of medical device robotics and automation [34]. Second, the small deformation model presented here is valuable in modeling processes in which large deformation does not occur, such as those seen during ablation [1] or interaction with wearable electronic devices.

5 Conclusion

Ultimately, a novel method for modeling the physics occurring within biological tissue interacting with external devices has been presented. Despite the weakness of assuming small deformations, the model was still able to predict temperature and water content occurring in tissue during arterial tissue fusion to within a standard deviation of experimentally measured data. To the authors' knowledge, while small deformation TPM models have been used to simulate geomechanical processes [16] and food processing [23,24], this is the first to do so for medical device interaction with biological tissue, providing an initial step toward all-encompassing, predictive models.

Acknowledgment

The authors would like to thank Alex O'Brien for his time and support during this study.

References

- [1] Berjano, E. J., 2006, "Theoretical Modeling for Radiofrequency Ablation: State-of-the-Art and Challenges for the Future," *Biomed. Eng. Online*, 5(1), p. 24.

- [2] Fankell, D. P., Kramer, E., Cezo, J., Taylor, K. D., Ferguson, V. L., and Rentschler, M. E., 2016, "A Novel Parameter for Predicting Arterial Fusion and Cutting in Finite Element Models," *Ann. Biomed. Eng.*, **44**(11), pp. 3295–3306.
- [3] Pearce, J. A., 2010, "Models for Thermal Damage in Tissues: Processes and Applications," *Crit. Rev. Biomed. Eng.*, **38**(1), pp. 1–20.
- [4] Tungjithkusolmun, S., Staelin, S. T., Haemmerich, D., Tsai, J.-Z., Cao, H., Webster, J. G., Lee, F. T., Mahvi, D. M., and Vorperian, V. R., 2002, "Three-Dimensional Finite-Element Analyses for Radio-Frequency Hepatic Tumor Ablation," *IEEE Trans. Biomed. Eng.*, **49**(1), pp. 3–9.
- [5] Datta, A. K., and Rakesh, V., 2010, *An Introduction to Modeling of Transport Processes: Applications to Biomedical Systems*, Cambridge University Press, Cambridge, UK.
- [6] Martin, C., Sun, W., and Elefteriades, J., 2015, "Patient-Specific Finite Element Analysis of Ascending Aorta Aneurysms," *Am. J. Physiol.: Heart Circ. Physiol.*, **308**(10), pp. H1306–H1316.
- [7] Karajan, N., 2012, "Multiphasic Intervertebral Disc Mechanics: Theory and Application," *Arch. Comput. Methods Eng.*, **19**(2), pp. 261–339.
- [8] Jin, Z., 2014, *Computational Modelling of Biomechanics and Biotribology in the Musculoskeletal System: Biomaterials and Tissues*, Elsevier, Philadelphia, PA.
- [9] Regueiro, R. A., Zhang, B., and Wozniak, S. L., 2014, "Large Deformation Dynamic Three-Dimensional Coupled Finite Element Analysis of Soft Biological Tissues Treated as Biphasic Porous Media," *Comput. Model. Eng. Sci.*, **98**(1), pp. 1–39.
- [10] Jayaraman, G., 1983, "Water Transport in the Arterial Wall—A Theoretical Study," *J. Biomech.*, **16**(10), pp. 833–840.
- [11] Chapelle, D., Gerbeau, J.-F., Sainte-Marie, J., and Vignon-Clementel, I. E., 2010, "A Poroelastic Model Valid in Large Strains With Applications to Perfusion in Cardiac Modeling," *Comput. Mech.*, **46**(1), pp. 91–101.
- [12] Diller, K. R., and Hayes, L. J., 1983, "A Finite Element Model of Burn Injury in Blood-Perfused Skin," *ASME J. Biomech. Eng.*, **105**(3), pp. 300–307.
- [13] Ehlers, W., and Bluhm, J., 2013, *Porous Media: Theory, Experiments and Numerical Applications*, Springer-Verlag, Berlin.
- [14] Bowen, R. M., 1980, "Incompressible Porous Media Models by Use of the Theory of Mixtures," *Int. J. Eng. Sci.*, **18**(9), pp. 1129–1148.
- [15] De Boer, R., 2005, *Trends in Continuum Mechanics of Porous Media*, Springer, Dordrecht, The Netherlands.
- [16] Wang, W., Regueiro, R. A., and McCartney, J. S., 2015, "Coupled Axisymmetric Thermo-Poro-Mechanical Finite Element Analysis of Energy Foundation Centrifuge Experiments in Partially Saturated Silt," *Geotech. Geol. Eng.*, **33**(2), pp. 373–388.
- [17] Holzapfel, G. A., 2000, *Nonlinear Solid Mechanics: A Continuum Approach for Engineering*, Wiley, Medford, MA.
- [18] Lewis, R. W., and Schrefler, B. A., 1999, *The Finite Element Method in the Static and Dynamic Deformation and Consolidation of Porous Media*, 2nd ed., Wiley, Medford, MA.
- [19] Coussy, O., 2004, *Poromechanics*, 2nd ed., Wiley, Chichester, UK.
- [20] Wang, W., 2014, "Coupled Thermo-Poro-Mechanical Axisymmetric Finite Element Modeling of Soil-Structure Interaction in Partially Saturated Soils," *Ph.D. dissertation*, University of Colorado Boulder, Boulder, CO.
- [21] Coleman, B. D., and Noll, W., 1963, "The Thermodynamics of Elastic Materials With Heat Conduction and Viscosity," *Arch. Ration. Mech. Anal.*, **13**(1), pp. 167–178.
- [22] Pearce, J., 2015, "Numerical Model Study of Radio Frequency Vessel Sealing Thermodynamics," *Proc. SPIE*, **9326**, p. 93260A.
- [23] Datta, A. K., 2007, "Porous Media Approaches to Studying Simultaneous Heat and Mass Transfer in Food Processes—II: Property Data and Representative Results," *J. Food Eng.*, **80**(1), pp. 96–110.
- [24] Halder, A., Dhall, A., and Datta, A. K., 2010, "Modeling Transport in Porous Media With Phase Change: Applications to Food Processing," *ASME J. Heat Transfer*, **133**(3), p. 031010.
- [25] Halder, A., Dhall, A., and Datta, A. K., 2007, "An Improved, Easily Implementable, Porous Media Based Model for Deep-Fat Frying—Part I: Model Development and Input Parameters," *Food Bioprod. Process.*, **85**(3), pp. 209–219.
- [26] Cezo, J., 2013, "Thermal Tissue Fusion of Arteries: Methods, Mechanisms, & Mechanics," *Ph. D. dissertation*, University of Colorado Boulder, Boulder, CO.
- [27] Cezo, J. D., Passernig, A. C., Ferguson, V. L., Taylor, K. D., and Rentschler, M. E., 2014, "Evaluating Temperature and Duration in Arterial Tissue Fusion to Maximize Bond Strength," *J. Mech. Behav. Biomed. Mater.*, **30**, pp. 41–49.
- [28] Cengel, Y., and Ghajar, A., 2010, *Heat and Mass Transfer: Fundamentals and Applications*, 4th ed., McGraw-Hill, New York.
- [29] Johnson, M., and Tarbell, J. M., 2000, "A Biphasic Anisotropic Model of the Aortic Wall," *ASME J. Biomech. Eng.*, **123**(1), pp. 52–57.
- [30] Chen, S. S., Wright, N. T., and Humphrey, J. D., 1997, "Heat-Induced Changes in the Mechanics of a Collagenous Tissue: Isothermal Free Shrinkage," *ASME J. Biomech. Eng.*, **119**(4), pp. 372–378.
- [31] Khalili, N., Uchaipichat, A., and Javadi, A. A., 2010, "Skeletal Thermal Expansion Coefficient and Thermo-Hydro-Mechanical Constitutive Relations for Saturated Homogeneous Porous Media," *Mech. Mater.*, **42**(6), pp. 593–598.
- [32] Chen, R. K., Chastagner, M. W., Dodde, R. E., and Shih, A. J., 2013, "Electrosurgical Vessel Sealing Tissue Temperature: Experimental Measurement and Finite Element Modeling," *IEEE Trans. Biomed. Eng.*, **60**(2), pp. 453–460.
- [33] Karšaj, I., and Humphrey, J. D., 2012, "A Multilayered Wall Model of Arterial Growth and Remodeling," *Mech. Mater. Int. J.*, **44**, pp. 110–119.
- [34] Marbán, A., Casals, A., Fernández, J., and Amat, J., 2014, "Haptic Feedback in Surgical Robotics: Still a Challenge," *ROBOT2013: First Iberian Robotics Conference*, Vol. 252, M. A. Armada, A. Sanfeliu, and M. Ferre, eds., Springer International Publishing, Cham, Switzerland, pp. 245–253.